Constraints on the neutron star equation of state from AT2017gfo using radiative transfer simulations

Michael W. Coughlin,[1]* Tim Dietrich,[2] Zoheyr Doctor,[3,4] Daniel Kasen,[5,6] Scott Coughlin,[7,8] Anders Jerkstrand,[9] Giorgos Leloudas,[10] Owen McBrien,[11] Brian D. Metzger,[12] Richard O'Shaughnessy[13] and Stephen J. Smartt[14]

[1]*Division of Physics, Math, and Astronomy, California Institute of Technology, Pasadena, CA 91125, USA*
[2]*Nikhef, Science Park 105, NE-1098 XG Amsterdam, the Netherlands*
[3]*Kavli Institute for Cosmological Physics, University of Chicago, Chicago, IL 60637, USA*
[4]*Department of Physics, University of Chicago, Chicago, IL 60637, USA*
[5]*Departments of Physics and Astronomy, and Theoretical Astrophysics Center, University of California, Berkeley, CA 94720, USA*
[6]*Nuclear Science Division, Lawrence Berkeley National Laboratory, Berkeley, CA 94720, USA*
[7]*Physics and Astronomy, Cardiff University, Cardiff CF10 2FH, UK*
[8]*Center for Interdisciplinary Exploration & Research in (CIERA), Northwestern University, Evanston, IL 60208, USA*
[9]*Max-Planck Institut für Astrophysik, Karl-Schwarzschild-Strasse 1, D-85748 Garching, Munich, Germany*
[10]*Dark Cosmology Centre, Niels Bohr Institute, University of Copenhagen, Juliane Maries Vej 30, DK-2100 Copenhagen, Denmark*
[11]*Astrophysics Research Centre, School of Mathematics and Physics, Queen's University Belfast, Belfast BT7 1NN, Northern Ireland, UK*
[12]*Department of Physics and Columbia Astrophysics Laboratory, Columbia University, New York, NY 10027, USA*
[13]*Center for Computational Relativity and Gravitation, Rochester Institute of Technology, Rochester, NY 14623, USA*
[14]*Astrophysics Research Centre, School of Mathematics and Physics, Queen's University Belfast, Belfast BT7 1NN, UK*

ABSTRACT

The detection of the binary neutron star merger GW170817 together with the observation of electromagnetic counterparts across the entire spectrum inaugurated a new era of multimessenger astronomy. In this study, we incorporate wavelength-dependent opacities and emissivities calculated from atomic-structure data enabling us to model both the measured light curves and spectra of the electromagnetic transient AT2017gfo. Best fits of the observational data are obtained by Gaussian Process Regression, which allows us to present posterior samples for the kilonova and source properties connected to GW170817. Incorporating constraints obtained from the gravitational wave signal measured by the LIGO-Virgo Scientific Collaboration, we present a 90 per cent upper bound on the mass ratio $q \lesssim 1.38$ and a lower bound on the tidal deformability of $\tilde{\Lambda} \gtrsim 197$, which rules out sufficiently soft equations of state. Our analysis is a path-finder for more realistic kilonova models and shows how the combination of gravitational wave and electromagnetic measurements allow for stringent constraints on the source parameters and the supranuclear equation of state.

Key words: atomic processes – gravitational waves.

1 INTRODUCTION

A new era of multimessenger astronomy began with the combined detection of a neutron star (NS) merger via the gravitational wave GW170817 (Abbott et al. 2017b), the gamma-ray burst (GRB) GRB170817A (Abbott et al. 2017e), and the electromagnetic (EM) transient AT2017gfo (Abbott et al. 2017d). The discovery of a bright optical and near-infrared source in NGC 4993, consistent with the gravitational-wave sky localization, during the first 12 h after the

joint gravitational wave and gamma-ray detections (Arcavi et al. 2017; Coulter et al. 2017; Lipunov et al. 2017; Soares-Santos et al. 2017; Tanvir et al. 2017; Valenti et al. 2017) led to intensive follow-up campaigns to show that this was an unusual and unprecedented transient emitting from the X-ray to radio (Alexander et al. 2017; Chornock et al. 2017; Cowperthwaite et al. 2017; Drout et al. 2017; Evans et al. 2017; Haggard et al. 2017; Hallinan et al. 2017; Kasliwal et al. 2017; Kilpatrick et al. 2017; Margutti et al. 2017; McCully et al. 2017; Nicholl et al. 2017; Pian et al. 2017a; Shappee et al. 2017; Smartt et al. 2017; Troja et al. 2017; Utsumi et al. 2017). This event showed that compact binary mergers including at least one NS can create an EM counterpart known as a *kilonova* (Lattimer &

* E-mail: mcoughli@caltech.edu

Schramm 1974; Li & Paczynski 1998; Metzger et al. 2010; Roberts et al. 2011; Kasen et al. 2017). Kilonovae originate from neutron-rich outflows from the merger that emit ultraviolet/optical/infrared emission powered by the radioactive decay of r-process elements. Kilonovae are of enormous scientific value: They offer insight into the equation of state (EOS) of NSs (Bauswein, Baumgarte & Janka 2013a; Abbott et al. 2017a; Bauswein et al. 2017; Radice et al. 2018), the formation of heavy elements (Just et al. 2015; Wu et al. 2016; Abbott et al. 2017f; Roberts et al. 2017) and the expansion rate of the universe (Abbott et al. 2017c).

While AT2017gfo is the only confirmed kilonova observed to date, there has been significant theoretical work on modelling the nature of these transients. These studies have postulated two main forms of ejecta from NS mergers: dynamical and wind ejecta. The dynamical ejecta is the matter expelled at the moment of the merger from tidal stripping of the NSs and from the NS–NS contact interface (e.g. Rosswog et al. 1999; Oechslin, Janka & Marek 2007; Bauswein, Goriely & Janka 2013b; Wanajo et al. 2014; Sekiguchi et al. 2015; Hotokezaka et al. 2016; Rosswog et al. 2017b; Wollaeger et al. 2018). Wind ejecta is produced through remnant accretion disc winds, which can be driven by neutrino energy, magnetic fields, viscous evolution and/or nuclear recombination energy (e.g. Fryer, Woosley & Hartmann 1999; Di Matteo et al. 2002; Metzger, Piro & Quataert 2008; Dessart et al. 2009; Fernández & Metzger 2013; Perego et al. 2014; Siegel, Ciolfi & Rezzolla 2014; Ciolfi & Siegel 2015; Just et al. 2015; Martinez et al. 2015; Rezzolla & Kumar 2015). The masses, velocities, and compositions of the different ejecta types can vary, which results in different observed kilonova morphology.

The UV–optical–near-infrared light curves and spectra of AT2017gfo have been used to infer ejecta mass, velocities, and compositions when combined with simple toy model approaches (e.g. those of Arnett 1982; Metzger 2017) and more sophisticated modelling of the few existing kilonova simulations (e.g. Kasen et al. 2017). The first papers published after the event which included quantitative modelling (Cowperthwaite et al. 2017; Kilpatrick et al. 2017; Smartt et al. 2017; Tanvir et al. 2017), and later papers based on combined data (Villar et al. 2017; Rosswog et al. 2017a; Perego, Radice & Bernuzzi 2017; Waxman et al. 2017) produced broadly similar results. All the analyses consistently found that a few hundredths of a solar mass was ejected in AT2017gfo at velocities between 0.1 and 0.3c. However, none of these studies performed fits or inference using full radiative-transfer simulations.

In this work, we build on these previous analyses by performing Bayesian inference on observed AT2017gfo photometry and spectra using 'surrogate' models that are trained on the outputs of radiative transfer simulations. The surrogate models allow one to calculate the likelihood of the data for any ejecta parameters and hence derive posterior distributions on those parameters. Additionally, we go beyond inferences of only ejecta properties and constrain the NS–binary parameters information from full numerical relativity simulations of NS mergers. The contribution of each type of ejecta and their mass, velocity, and composition are expected to depend on the parameters of the compact binary, the compact object masses, spins, orbital eccentricity, as well as the properties of NSs, such as the EOS (Rosswog et al. 1999; Bauswein et al. 2013b; Hotokezaka et al. 2013; Lehner et al. 2016; Radice et al. 2016; Dietrich & Ujevic 2017; Abbott et al. 2017f; Siegel & Metzger 2017). As such, observed kilonova emission can be used to constrain the compact binary parameters (or vice versa) using a mapping from ejecta properties to NS–binary parameters (Abbott et al. 2017a; Coughlin et al. 2017). Of particular interest is the EOS of cold supranuclear matter,

since it was constrained by the GW170817 signal (Abbott et al. 2017b) and can be independently constrained by the electromagnetic data (Radice et al. 2018).

The layout of this paper is as follows: First, we describe the data set used for our analysis. Then, we discuss our method for interpolating the output of kilonova simulations over the full parameter space of ejecta mass, velocity, and composition and describe the Bayesian procedure for inferring ejecta properties of AT2017gfo from the photometry. Finally, we use the measured ejecta properties to put new constraints on the NS EOS and the GW170817 binary mass ratio.

2 DATA

A massive photometric data set was gathered with intra-day time resolution by many teams with latitudinally separated observatories in the southern hemisphere and in Hawaii. We compiled our own selected set of photometry and recalculated bolometric luminosities with realistic error bars. We began with the photometry from the UV to *K* band from (Andreoni et al. 2017; Arcavi et al. 2017; Chornock et al. 2017; Cowperthwaite et al. 2017; Drout et al. 2017; Evans et al. 2017; Kasliwal et al. 2017; Tanvir et al. 2017; Pian et al. 2017a; Troja et al. 2017; Smartt et al. 2017; Utsumi et al. 2017; Valenti et al. 2017) from phases +0.467 to +25.19 d after GW170817 and at each epoch created the broadest spectral energy distribution possible. Data from the *Swift* satellite in UV bands were only available from Evans et al. (2017) until +1 d and the last *U*-band detection is from Smartt et al. (2017) at +1.505 d. No secure optical data are available after epoch +11.3 d when AT2017gfo faded below 24 mag in *g* band, and the transient is only detected in *H* and K_s until +14.3 d and then only K_s thereafter.

We began with the photometry of Smartt et al. (2017) as the core data set and employed difference imaging at all epochs of PESSTO (Public ESO Spectroscopic Survey of Transient Objects; Smartt et al. 2015), GROND, and Pan-STARRS imaging. Our approach was to (i) complement this photometry only when this was necessary either due to insufficient temporal or wavelength coverage, (ii) primarily use only *grizyJHK*$_S$ AB mag photometry from sources that used image subtraction (mostly DECam and Skymapper Cowperthwaite et al. 2017; Andreoni et al. 2017), or from *HST* where host contamination is not important (Tanvir et al. 2017), and (iii) when this was not possible, focus on a small number of independent sources such as Gemini South (Kasliwal et al. 2017), VISTA (Tanvir et al. 2017), and Sirius (Utsumi et al. 2017). We verified consistency between the data sets through direct comparison. In this way, we compiled *grizyJHK*$_S$ SEDs, or as broad a subset as the data allowed. From the first detection at 0.47 d, there are five distinct epochs within the first 24 h (including Swift satellite data) at which L_{bol} can be calculated. A total of 20 distinct epochs with enough data to define a black body fit can be defined up to +10.4 d after GW170817. We note that our GROND *K*-band photometry has been updated compared to Smartt et al. (2017). This is because the GROND template for host subtraction still contained flux from the transient (as first noted by Villar et al. 2017). The image subtraction has now been redone using a different template with no flux present and after this correction, the present GROND light-curve matches much better with other *K*-band measurements in the literature. The recommended updated photometry values are now published and available on the PESSTO webpage[1] and we employ them here. We

[1] www.pessto.org

used this *ugrizyJHK*$_S$ compilation to constrain the model fits as discussed below.

We have used these data to calculate the bolometric luminosities from +0.467 to +13.21 d,[2] after which the wavelength coverage is insufficient to securely determine L_{bol}. The bolometric light curves are given in the table in the Supplementary Materials and their construction in the Supplementary Materials. Manual comparison of the models of Kasen et al. (2017) showed some promising agreement with the near infra-red spectrum of Chornock et al. (2017) at +2.5 to +4.5 d in particular, although only the 1.0–1.8 µm region was compared and the evolution was not consistently reproduced. It is clear that the X-shooter spectra of Pian et al. (2017b) and Smartt et al. (2017) taken with ESO's Very Large Telescope contain all available spectral information since they cover 0.35–2.5 µm on a daily basis from +1.5 to +10.5 d. This is an excellent data set to more rigorously constrain the ejecta properties. We employed the reduced X-Shooter spectra made publicly available on WISeREP[3] and through PESSTO.[1] We do not use any other spectral data set, as other data are inferior signal-to-noise ratio, reduced wavelength coverage, or both, and after +1.5 d, no other spectral data set provides additional temporal information that enhances the X-shooter sequence in any way.

3 KILONOVA SURROGATE MODEL

Throughout this work, we use the kilonova models presented in Kasen et al. (2017) that employ a multidimensional Monte Carlo code to solve the multiwavelength radiation transport equation for a relativistically expanding medium. Initial use of the model and comparison to data showed promising similarities with some epochs of near infra-red spectra (Chornock et al. 2017) and the bolometric luminosity (Kilpatrick et al. 2017). Until now a comparison with the full wavelength and temporal spectral series (X-Shooter spectra from Pian et al. 2017b; Smartt et al. 2017) has not been done, but is essential to extract additional details about the ejecta (Rosswog et al. 2017a; Smartt et al. 2017; Waxman et al. 2017). Here, we will employ all of the data published to date to constrain the model fits.

The Kasen et al. (2017) models depend parametrically on the ejecta mass M_{ej}, the mass fraction of lanthanides X_{lan}, and the ejecta velocity v_{ej}. In terms of the underlying physics of the merger and ejecta processes described above, these three parameters would be determined by the detailed ejecta processes involved, e.g. the duration of the outflow, mass involved, and nucleosynthesis allowed, given the outflow trajectory and neutrino illumination sources. In this work, eschewing detailed neutrino radiation hydrodynamic simulations of mergers, we treat these properties as parameters. We can use separate one-component models to create a two-component ejecta model by summing together two one-component models. This sum is performed by first generating the bolometric light curves, photometric light curves, and spectra for the individual models. The two-component bolometric light curves and spectra are produced by simply adding the one-dimensional (1D) curves together, while the photometric light curves are added in the way appropriate for log-based quantities. The use of a two-component model is motivated by the theoretical prediction of the presence of different ejecta components and also by the fact that the ejecta are observed to fade rapidly in the UV and optical but have a significantly different near-infrared evolution. We restrict our analysis to spherical symmetry and a uniform composition, and neglect mixing of different ejecta types (Rosswog et al. 2017b) when we add the two separate model components. The expansion of the model to non-spherical geometries and compositional gradients is left for future analyses.

The model provided in Kasen et al. (2017) and described above is produced on a grid with ejecta masses $M_{ej}[M_\odot] = 0.001, 0.0025, 0.005, 0.0075, 0.01, 0.25, 0.05,$ and 0.1, ejecta velocities $v_{ej}[c] = 0.03, 0.05, 0.1, 0.2,$ and 0.3, and mass fraction of lanthanides $X_{lan} = 0, 10^{-5}, 10^{-4}, 10^{-3}, 10^{-2},$ and 10^{-1}. The models have temporal epochs of 0.1 d sampling. In order to draw inferences about generic sources not corresponding to one of these gridpoints, we develop a novel method to create a parameterized model from a set of numerical data. We adapt the approach outlined in Doctor et al. (2017) and Pürrer (2014), where Gaussian Process Regression (GPR) is employed to interpolate principal components of gravitational waveforms based on existing sets of simulations. In this analysis, we perform a similar computation but on bolometric luminosities, light curves in standard filters, and spectra. The details of the algorithm to perform the interpolation can be found in the Supplementary Materials. We also explore in the Supplementary Materials the question of whether there are enough simulations on the grid in order to draw inferences based on the model. We show by removing a simulation from the grid and comparing the resulting interpolated light curves and spectra to that simulation that the grid is dense enough to reproduce the simulation.

4 ANALYSIS

We use the Bayesian procedure described in Coughlin et al. (2017) to compare our GPR-based kilonova bolometric, photometric, and spectral models with the full observational data set and draw posterior inferences about our model parameters v_{ej}, M_{ej}, and X_{lan}. For each component, the flat priors used in our analysis cover the region $-5 \leq \log_{10}(M_{ej}/M_\odot) \leq 0$, $0 \leq v_{ej} \leq 0.3c$, and $-9 \leq \log_{10}(X_{lan}) \leq -1$. In all cases, the likelihood is based on the χ^2 value between our model and the data. For the two-component models, we require $X_{lan1} > X_{lan2}$ and $v_1 < v_2$. The velocity prior is employed to limit to systems where the blue ejecta is ahead of the red ejecta, which is the regime for this non-interacting model to be valid. The order of the components does reflect their lanthanide fraction, with a large X_{lan} corresponding to a red, lanthanide-rich component and a small X_{lan} to a blue, lanthanide-poor component. In fact, in the 1D picture that we consider here, the blue component cannot be at lower velocity than the red physically because the latter would not allow its emission to escape.

We now discuss this prior choice and the origin of the blue and red components of the kilonovae. In general, there are two options. The first is that the ejecta is to a reasonable approximation isotropic, with a blue component everywhere ahead and faster than the red one. In this case, the present treatment of the multicomponent model is appropriate, and all the conclusions derived are consistent. There are reasons to expect this may be the case in certain regimes. First proposed by Metzger & Fernandez (2014), it was thought the only source of the blue ejecta was from the disc wind in the case of a long-lived hypermassive NS and the red ejecta might arise from the tidal tail or a disc wind. The early spectral observations (McCully et al. 2017; Nicholl et al. 2017; Shappee et al. 2017; Smartt et al. 2017) suggest the blue component is moving relatively fast ($\approx 0.3\,c$) that is likely faster than a standard disc wind would produce, motivating its potential association with dynamical ejecta. This motivates our prior choice.

---

[2] We use the data up to 10 d when calculating the fits.
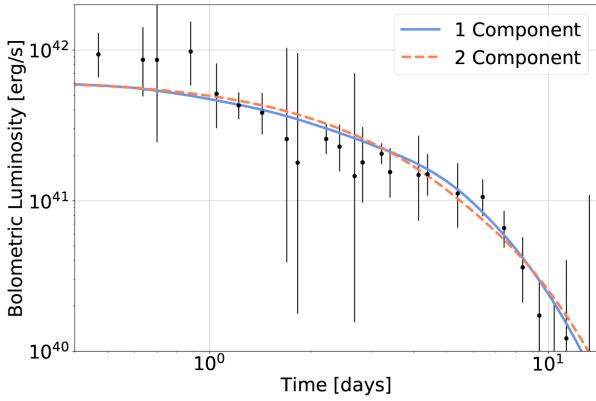[3] https://wiserep.weizmann.ac.il

Figure 1. Derived bolometric luminosity and a maximum likelihood χ^2 fit using the one- and two-component kilonova bolometric luminosity models of Kasen et al. (2017). We provide the L_{bol} data in the Supplementary Materials.

There is also the possibility that the ejecta is significantly anisotropic or there are significant interactions between different components or with a possible expanding jet. In general, a two-component model where the components are allowed to interact would be required in this case, although the assumption above is valid in the case that the ejecta is observed from a specific direction such that the lanthanide-free component is ahead of and faster than the red one. The velocity constraints will not be valid if the red and blue components originate from geometrically distinct regions, e.g. if the blue comes out in the polar direction and the red comes out in the equatorial plane. For example, it has been shown that the polar dynamical ejecta could itself be blue (Wanajo et al. 2014; Sekiguchi et al. 2015). In addition, no numerical relativity simulations have produced ejecta masses seen from AT2017gfo ($\approx 0.05\,M_\odot$) in the tidal tail component, while this quantity of red ejecta can readily come from the disc wind in the case that the hypermassive NS is relatively short lived (Siegel & Metzger 2017). Recently, Kawaguchi, Shibata & Tanaka (2018) used two-dimensional (2D) radiative transfer models to show that the potentially anisotropic properties of the ejecta requires less dynamical and Lanthanide-free ejecta to reproduce AT2017gfo, reducing the tension with numerical relativity simulations. Qualitatively, similar results were seen in other studies using 2D models (Wollaeger et al. 2018), and in semi-analytical models that explicitly take into account the non-spherical character of the ejecta (Perego et al. 2017). Another possibility is a two-component disc wind (e.g. Shibata et al. 2017). In this case, a fast, blue component is found for the outer torus ejection and a slow red component for the inner. For this reason, the results derived in the following rely on the assumption that the blue component is everywhere ahead and faster than the red one, which may not be the case.

To validate our analysis procedure, we first reproduce previous bolometric and photometric analyses of this event. The first test is to reproduce the analysis in Smartt et al. (2017), where the bolometric light curves were computed from the available photometry at that time. We fit our bolometric models to the bolometric data from Smartt et al. (2017) using a χ^2 likelihood. As shown in Fig. 1, both the one-component and two-component models can reproduce the measured bolometric luminosity. Although within error bars, the predicted bolometric luminosities are systematically low at early times. Based on the one-component fit to the bolometric luminosity, we estimate $\log_{10}(M_{ej}) = -1.39$ ($M_{ej} = 0.041\,M_\odot$), with a velocity

of $v_{ej} = 0.14c$ and a mass fraction of lanthanides of $X_{lan} = 10^{-6.41}$ (see Table 1 for error bars and the Supplementary Materials for the associated corner plots). Overall, this is consistent with Smartt et al. (2017) who found similar ejecta masses and velocities for a composition with an effective grey opacity of $\kappa \sim 0.1\,\mathrm{cm^2\,g^{-1}}$. Uncertainties in the atomic data render the conversion between opacity and lanthanide mass fraction non-trivial. However previous studies have shown that at $X_{lan} \sim 10^{-1}$ models have an effective grey opacity of $\kappa \sim 10$, while $X_{lan} \leq 10^{-6}$ models have an opacity closer to $\kappa \sim 0.1$, with the dependence being roughly logarithmic ($\kappa \propto [\log X_{lan}]^\alpha$). Employing a two-component model fit to L_{bol} makes a consistent prediction for the light curve and results in a total ejected mass of $M_{ej} = 0.054\,M_\odot$. While we can measure the total amount of ejecta by using only the bolometric information, the amount of matter in each component (and their composition) is ill determined (see the top row of the corner plots in the Supplementary Materials).

Increasing the complexity of the analysed data, we fit the broadband photometry points described earlier and illustrated in Fig. 2. We assign model uncertainties of 1 mag added in quadrature with the statistical error in the measured photometry (Coughlin et al. 2017). In general, the 1 mag uncertainties, which are treated as 1σ errors, are designed to capture difficult-to-quantify systematic uncertainties, such as those in the electron fraction and heating rate, which can lead to significant differences in the predicted luminosities (Rosswog et al. 2017b). Fitting the light curves with a single-component results in $\log_{10}(M_{ej}/M_\odot) = -1.41$ ($M_{ej} = 0.040\,M_\odot$), consistent with our previous findings. However, for early times (<4 d) the model does not allow a representation of the H, and K bands and the predicted g band is not consistent within the assigned uncertainties after 4 d. Conversely, a two-component model (blue shaded region) can reproduce both early and late-time behaviour in all bands. Using photometric data, we can distinguish between the two types of ejecta with different velocities and lanthanide fractions. These two components are not strongly differentiated using bolometric information alone. In our two-component photometric analysis, we find that the more massive ejecta component has a higher lanthanide fraction. The amount of blue (lanthanide-poor) ejecta is also notable, $\log_{10}(M_{ej}/M_\odot) = -1.59$ ($M_{ej} = 0.026\,M_\odot$), forming a significant fraction of the total ejecta. We return to the implications for this in the summary.

For the first time, we will also compare the spectra of AT2017gfo against theoretical kilonova predictions to compute posteriors. As discussed in Pian et al. (2017b) and Smartt et al. (2017), the first X-Shooter and PESSTO EFOSC2 spectra are bright and blue, with rapid cooling just a day later. We fit the spectra of AT2017gfo directly (Pian et al. 2017b; Smartt et al. 2017) in Fig. 3. In line with the uncertainties of the photometric light curves, we use an upper error bar of $2.5\times$ the spectral value and a lower error bar of $1/2.5\times$ the spectral value. This model uncertainty is added in quadrature with the statistical error in the measured spectra. Except for the early epoch when the predicted spectra declines slightly too quickly in the red, broad agreement in the overall shape between the kilonova model and the X-shooter spectra is obtained. Indeed, the model reproduces the spectra within the estimated uncertainty. The fit to the spectra results in $\log_{10}(M_{ej}/M_\odot) = -1.48$ ($M_{ej} = 0.033\,M_\odot$) for a single component, and $\log_{10}(M_{ej1}/M_\odot) = -2.03$ ($M_{ej} = 0.010\,M_\odot$), $\log_{10}(M_{ej2}/M_\odot) = -1.63$ ($M_{ej} = 0.023\,M_\odot$) for the two component model. Overall, we find that the ejecta properties based on the light curves and based on the spectra are very similar. This shows that at the level of model uncertainties considered here, for a successful kilonovae model, it is possible to use

Table 1. Ejecta properties estimated from the GPR. The estimated uncertainties give the 1σ uncertainty. Corner plots from which these numbers are derived are shown in the Supplementary Materials. The two-component model lists the higher lanthanide fraction as X_{lan1} and lower as X_{lan2} (corresponding to dynamical and wind components).

	Bolometric luminosity		Light curve		Spectra	
	One component	Two component	One component	Two component	One component	Two component
$\log_{10}(M_{ej1}/M_{\odot})$	$-1.39^{+0.13}_{-0.11}$	$-2.50^{+1.06}_{-1.60}$	$-1.30^{+0.10}_{-0.13}$	$-1.51^{+0.23}_{-0.13}$	$-1.48^{+0.13}_{-0.14}$	$-2.03^{+0.56}_{-1.02}$
v_{ej1} (c)	$+0.12^{+0.09}_{-0.06}$	$+0.09^{+0.09}_{-0.06}$	$+0.23^{+0.06}_{-0.16}$	$+0.10^{+0.08}_{-0.06}$	$+0.20^{+0.003}_{-0.004}$	$+0.10^{+0.08}_{-0.05}$
X_{lan1}	$-6.77^{+1.80}_{-1.30}$	$-2.18^{+1.56}_{-1.16}$	$-3.54^{+0.39}_{-0.36}$	$-1.61^{+0.96}_{-1.04}$	$-2.97^{+0.30}_{-0.39}$	$-1.52^{+0.97}_{-0.98}$
$\log_{10}(M_{ej2}/M_{\odot})$	–	$-1.39^{+0.13}_{-0.63}$	–	$-1.59^{+0.16}_{-0.18}$	–	$-1.63^{+0.20}_{-0.34}$
v_{ej2} (c)	–	$+0.20^{+0.05}_{-0.08}$	–	$+0.17^{+0.09}_{-0.10}$	–	$+0.20^{+0.03}_{-0.01}$
X_{lan2}	–	$-3.91^{+0.73}_{-0.72}$	–	$-4.73^{+0.41}_{-0.20}$	–	$-3.31^{+0.50}_{-0.77}$

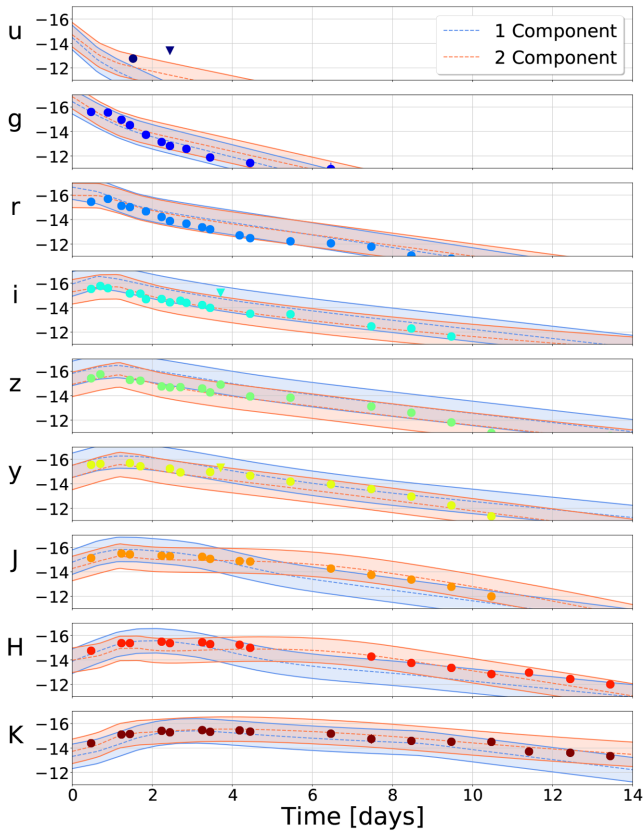**Figure 2.** Light curves for both one- and two-component models from Kasen et al. (2017). The shown light curves correspond to a maximum likelihood χ^2 fit to the data. Shaded regions represent the assumed 1 mag error budget. The source of the photometry is summarized in Section 2.

either the light curves or the spectra, but the integrated information of the bolometric luminosity are insufficiently informative to constrain ejecta properties. We show in the Supplementary Materials that spectra based on the light-curve fits (and vice versa) give reasonable fits as well.

5 INFERRING SOURCE PROPERTIES

Finally, we want to use our analysis to obtain information about the binary parameters, such as the total mass, mass ratio, and tidal deformability. The idea follows the discussion in Coughlin et al. (2017): namely that information about the ejecta properties can be translated to constraints on the system parameters by fits such as

those from Dietrich & Ujevic (2017). In this work, we improve on the fit of Dietrich & Ujevic (2017), which connects the intrinsic binary parameters with dynamical ejecta properties extracted from full 3D numerical relativity simulations. These new fits are described in the Supplementary Materials. We emphasize that numerical relativity simulations do not extend significantly past the moment of merger, and so they cannot capture the wind-driven ejecta expected at later times. We therefore for this study assume that the total ejecta mass is parametrized by the total ejected mass given by numerical relativity simulations with a scale factor such that

$$M_{ej} = A \times M_{ej}^{NR} \qquad \text{with } A > 1. \tag{1}$$

We sample uniform in A with broad enough priors so as to not affect the posteriors such that we only restrict $A \times M_{ej}^{NR}$ to be less than the total mass.

This fit allows us to directly tie the measured ejecta mass and velocity to properties of the binary, including the mass ratio and EOS. Based on this fit and the numerical relativity simulations that underlie it, the total amount of dynamical ejecta will be largest when the NS involved are less compact. Therefore, based on our estimates for the total amount of ejecta required to explain the kilonova as reported in Table 1, we expect that a self-consistent analysis of EM and GW data will disfavour NSs that are too compact and hence allow us to constrain the nuclear EOS.

Incorporating information from gravitational-wave parameter estimation, namely a chirp mass M_c of $M_c = 1.188\,M_{\odot}$ (Abbott et al. 2017b) and an upper limit on the tidal deformability of $\tilde{\Lambda} \lesssim 640$,[4] we are able to place constraints on the mass ratio and tidal deformability of the system. Fig. 4 summarizes our findings. We find that the mass ratio of GW170817 is with 90 per cent confidence smaller than $q \lesssim 1.38$, while the 90 per cent lower bound on the tidal deformability is $\tilde{\Lambda} \gtrsim 197$. This lower bound shows that more compact EOSs such as WFF1 are disfavoured (see Fig. 4). These results can be compared to estimates obtained from a reanalysis of GW170817 (De et al. 2018), which incorporates quasi-universal relations for the tidal deformability and obtains 90 per cent lower bounds on the tidal deformability $\tilde{\Lambda} \gtrsim 117$ and 90 per cent upper bounds on the mass ratio $q \lesssim 1.51$. Our analysis shows that even without the use of quasi-universal relations tighter constraints on the binary parameters can be obtained from EM observations if bounds on the tidal deformability and the chirp mass can be inferred from

---

[4]The exact value of $\tilde{\Lambda} \lesssim 640$ arises from the fact that as stated in Abbott et al. (2017b) an analysis of GW170817 with the SEOBNRv4_ROM_NR tidal waveform model Bohe et al. (2017); Dietrich, Bernuzzi & Tichy (2017); Dietrich et al. (2018) gives an 80 per cent tighter bound than the PN-based Taylor F2 model for which $\tilde{\Lambda} = 800$ was stated.
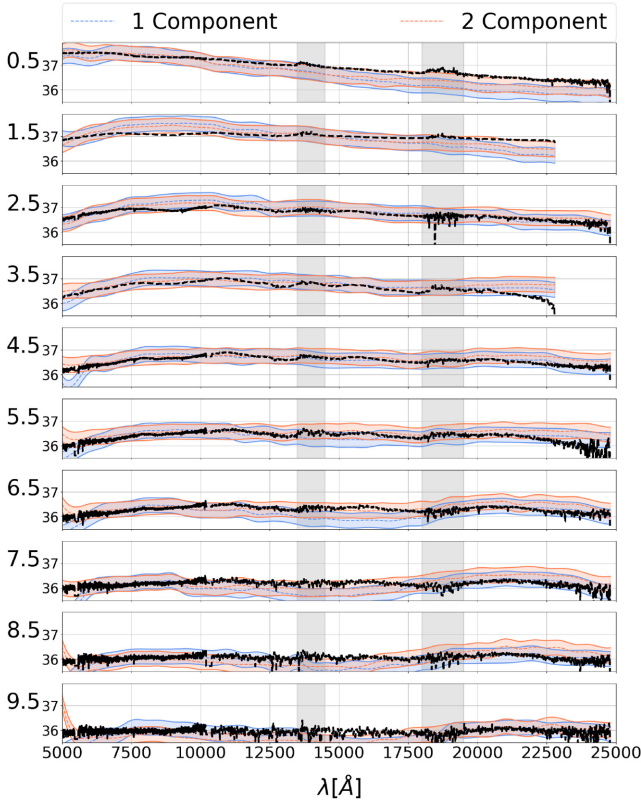
Figure 3. X-shooter spectra (black lines) in units of log10(erg s^{-1} A^{-1}) at the available epochs (in units of days on the far left) and one- and two-component model fits to the spectra (Pian et al. 2017b; Smartt et al. 2017). The shown spectra correspond to a maximum likelihood χ^2 fit to the data. Shaded regions correspond to an assumed 1 mag error budget. The grey shaded regions mark ignored regions due to atmospheric transmission.
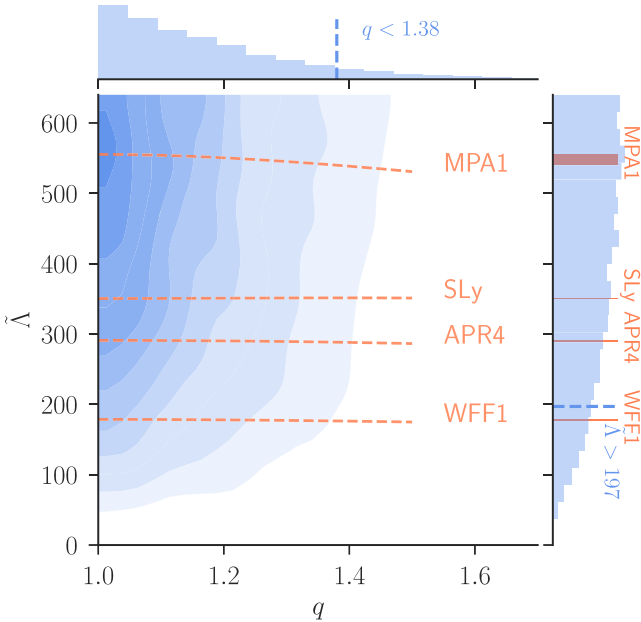

Figure 4. Corner plot for the constraining the mass ratio q, and tidal deformability $\tilde{\Lambda}$ assuming a chirp mass of $M_c = 1.188\,\mathrm{M_\odot}$ and based on the ejecta estimated obtained from the light-curve fitting. We include estimates for the tidal deformability for a set of possible EOSs as orange lines showing that too soft EOSs are ruled out by our analysis. The numbers represent the 90 per cent limits on the parameters.

GW astronomy. Although broadly consistent, we obtain a more conservative lower bound on the tidal deformability than Radice et al. (2018), who find lower bounds of $\tilde{\Lambda} \gtrsim 400$ to form discs and ejecta massive enough to create bright EM observables. On the other hand, the radius constraint derived in Bauswein et al. (2017) is in great agreement with our result, since Bauswein et al. (2017) arrive at $\tilde{\Lambda} > 210$. Additionally, also a comparison against Annala et al. (2018) and Most et al. (2018) that obtain, respectively, lower bounds on the tidal deformability of 120 and 375 (2σ value) for a 1.4 solar mass NS is possible. Annala et al. (2018) and Most et al. (2018) base their results on constraints obtained from GW170817 and state-of-the-art nuclear physics considerations. While in particular Most et al. (2018) obtains a more stringent bound, very similar to the one of Radice et al. (2018), this result is in agreement with ours since the bound of Most et al. (2018) is based on a large set of possible EOSs and gives credible interval with respect to this comparison set of EOSs and not on the direct measurement of GW170817 or AT2017gfo as done in this work. In addition to q and $\tilde{\Lambda}$, our analysis also allows us to estimate the amount of dynamical ejecta. We find that only 10 per cent of the total amount of ejecta is dynamical ejecta, which supports the idea that the bulk of the ejecta comes from disc outflows (Metzger et al. 2008).

6 SUMMARY

In this article, we obtained constraints on the GW170817 progenitor's mass ratio and tidal deformability, which are more stringent than those obtained purely from gravitational-wave observations. The unknown EOS can be constrained once information of the observed GW and EM signals are combined. To our knowledge, the presented analysis is the first study constraining the source properties of GW170817 and EOS with statistical methods modelling the light curve and spectra of AT2017gfo with surrogate models of radiative transfer simulations [see e.g. Bauswein et al. (2017); Radice et al. (2018) for alternative approaches combining EM and GW information].

Concentrating on the light-curve fits, given that the broadband colours are the most robustly modelled, a two-component fit is favoured over a one-component fit, although the single-component fit still broadly reproduces the photometric light curves well. The single-component fit is consistent with a large ejecta mass $M_{\rm ej} \approx 0.05\,\mathrm{M_\odot}$ and blue (lanthanide-poor) component ($X_{\rm lan} \approx 3 \times 10^{-4}$). The velocity distribution is broad and slightly bi-modal, partially favouring a low velocity ($v_{\rm ej} \approx 0.06c$) and partially a high ($v_{\rm ej} \approx 0.3c$).

For the two-component fit, our findings of a relatively large ejecta mass $M_{\rm ej} \approx 0.03\,\mathrm{M_\odot}$, and low velocity $v_{\rm ej} \approx 0.1c$, for the red (lanthanide-rich) component of the ejecta support its origin as being an outflow from the post-merger accretion disc (Metzger et al. 2008; Fernández & Metzger 2013; Just et al. 2015; Siegel & Metzger 2017), in agreement with previous interpretations of the KN emission from GW170817 (e.g. Chornock et al. 2017; Cowperthwaite et al. 2017; Kasen et al. 2017; Villar et al. 2017; Radice et al. 2018). Three-dimensional magnetohydrodynamic (MHD) simulations imply that ≈ 40 per cent of the newly formed torus can be ejected in winds at typical speeds $v_{\rm ej} \approx 0.1c$ (Siegel & Metzger 2017), such that the large inferred ejecta mass for GW170817 is explained by a relatively massive torus, $\approx 0.1\,\mathrm{M_\odot}$. GR simulations show that the latter is a fairly generic outcome of the merger process if the merger remnant first goes through a hypermassive NS phase (e.g. Shibata & Taniguchi 2006), and thus our observations disfavour a prompt collapse (see also Bauswein et al. 2017; Margalit & Metzger 2017).

On the other hand, whether the inferred lanthanide mass fraction is sufficient to explain the details of the solar system *r*-process abundance pattern (which requires $X_{lan} \approx 0.03-0.1$) is less clear; our results depend on the assumption of spherical symmetry, which could overestimate the amount of lanthanide-free ejecta.

By contrast, we infer that the blue (lanthanide-poor) component of the ejecta possesses a somewhat higher velocity $v_{ej} \gtrsim 0.2c$ and a similar ejecta mass $M_{ej} \approx 0.025\,M_\odot$ than the red component. While the velocity scale of the blue ejecta naturally matches expectations for the dynamical ejecta (e.g. Bauswein et al. 2013b; Hotokezaka et al. 2013), the relatively large quantity that we infer appears in tension with current GR merger simulations that focus on dynamical ejection mechanism. This may point to an alternative source of blue ejecta, such as the magnetized neutrino-irradiated wind from a long-lived hypermassive NS remnant prior to its collapse to a black hole (Metzger, Thompson & Quataert 2018; a purely neutrino-driven outflow is insufficient to explain the observed properties; Dessart et al. 2009). Alternatively, as with the red ejecta, the blue ejecta could originate from an accretion disc outflow (e.g. Metzger & Fernandez 2014; Perego et al. 2014); however, the high velocity is incompatible with both hydrodynamical and MHD simulations (e.g. Fan, Messenger & Heng 2014; Siegel & Metzger 2017).

Some of the blue light seen at the earliest epoch $\lesssim 1$ d could in principle also be attributed to physical effects not included in our modelling, such as the decay of free neutrons in the outermost fastest parts of the ejecta (Kulkarni 2005; Metzger et al. 2015), or additional thermal energy added to the ejecta by a relativistic jet ['cocoon' emission (Gottlieb et al. 2018; Kasliwal et al. 2017; Piro & Kollmeier 2018), however, see Duffell et al. (2018), who find that relatively little thermal energy is imparted to the ejecta to power early blue emission in the case of a successful GRB jet] or by internal shocks within whatever variable and temporally extended source (magnetar wind or accretion disc outflow) produces the KN ejecta (Metzger et al. 2018). As already discussed, we cannot exclude that up to ~10 per cent of the ejecta ($\lesssim 6 \times 10^{-3}\,M_\odot$) is dynamical in origin and instead could originate, e.g. from the tidal tail. The tidal tail ejecta is predicted to be fast ($v_{ej} \approx 0.2-0.3c$) and lanthanide-rich ($X_{lan} \gtrsim 0.03$), and its contribution to the light curve may be swamped by other components in the case of NS–NS mergers; prospects are better for unambiguously detecting this component in a NS–BH merger (e.g. Foucart et al. 2017).

Further work is needed due to possible systematic uncertainties introduced by the computation of the ejecta mass in numerical relativity simulations (Abbott et al. 2017f; Coughlin et al. 2017; Dietrich & Ujevic 2017) and the assumptions of our light curves as the restriction to spherical geometry. Since opacity and velocity control the diffusion time of the ejecta, the different ejecta channels have different characteristic magnitude, colour, and durations. This is further complicated by the fact that the observed colour is viewing angle dependent (Kasen, Fernandez & Metzger 2015) and that dynamical ejecta can have a gravitationally bound component falling back on to the central object, interacting with the outflow and altering the mass ejection and composition of the disc. Fernández et al. (2015) showed that the disc outflow suppresses fallback accretion, and Fernández et al. (2017) extended this analysis by varying the relative mass ratios of the ejecta by changing the density of the dynamical ejecta. Furthermore, the accuracy of current radiative transfer models in predicting kilonova colours still needs to be fully investigated, and more work is needed to improve atomic line lists, transfer physics, and thermalization (Kasen, Badnell & Barnes 2013; Tanaka 2016; Mao, Kaastra & Badnell 2017). Nevertheless, we have shown how the light curve and spectra can be robustly modelled and how parameter estimation pipelines can be employed to determine the source properties from the EM observations.

The light curves used in this analysis are publicly available at https://github.com/dnkasen/Kasen_Kilonova_Models_2017. The light curve fitting code is available at https://github.com/mcoughlin/gwemlightcurves.

REFERENCES

Abbott B. P. et al., 2017a, Phys. Rev. Lett., 119, 141101
Abbott B. P. et al., 2017b, Phys. Rev. Lett., 119, 161101
Abbott B. P. et al., 2017c, Nature, 551, 85
Abbott B. P. et al., 2017d, ApJ, 848, L12
Abbott B. P. et al., 2017e, ApJ, 848, L13
Abbott B. P. et al., 2017f, ApJ, 850, L39
Alexander K. D. et al., 2017, ApJ, 848, L21
Andreoni I. et al., 2017, PASA, 34, e069
Annala E., Gorda T., Kurkela A., Vuorinen A., 2018, Phys. Rev. Lett., 120, 172703
Arcavi I. et al., 2017, Nature, 551, 64
Arnett W. D., 1982, ApJ, 253, 785
Bauswein A., Baumgarte T. W., Janka H.-T., 2013a, Phys. Rev. Lett., 111, 131101
Bauswein A., Goriely S., Janka H.-T., 2013b, ApJ, 773, 78
Bauswein A. et al., 2017, ApJ, 850, L34
Bohe A. et al., 2017, Phys. Rev. D, 95, 044028
Chornock R. et al., 2017, ApJ, 848, L19
Ciolfi R., Siegel D. M., 2015, ApJ, 798, L36
Coughlin M., Dietrich T., Kawaguchi K., Smartt S., Stubbs C., Ujevic M., 2017, ApJ, 849, 12
Coulter D. A. et al., 2017, Science, 358, 1556
Cowperthwaite P. S., et al., 2017, ApJ, 848, L17
De S., Finstad D., Lattimer J. M., Brown D. A., Berger E., Biwer C. M., 2018
Dessart L., Ott C., Burrows A., Rosswog S., Livne E., 2009, ApJ, 690, 1681
Di Matteo T., Perna R., Narayan R., 2002, ApJ, 579, 706
Dietrich T., Ujevic M., 2017, Class. Quant. Grav., 34, 105014
Dietrich T., Bernuzzi S., Tichy W., 2017, Phys. Rev. D, 96, 121501
Dietrich T. et al., 2018
Doctor Z., Farr B., Holz D. E., Pürrer M., 2017, Phys. Rev. D, 96, 123011
Drout M. R. et al., 2017, Science, 358, 1570
Duffell P. C., Quataert E., Kasen D., Klion H., 2018, preprint (arXiv:1806.10616)
Evans P. A. et al., 2017, Science, 358, 1565
Fan X., Messenger C., Heng I. S., 2014, ApJ, 795, 43
Fernández R., Metzger B. D., 2013, MNRAS, 435, 502
Fernández R., Quataert E., Schwab J., Kasen D., Rosswog S., 2015, MNRAS, 449, 390
Fernández R., Foucart F., Kasen D., Lippuner J., Desai D., Roberts L. F., 2017, Classical and Quantum Gravity, 34, 154001
Foucart F. et al., 2017, Class. Quantum Gravity, 34, 044002

Fryer C. L., Woosley S. E., Hartmann D. H., 1999, ApJ, 526, 152

Gottlieb O., Nakar E., Piran T., Hotokezaka K., 2018, MNRAS, 479, 588

Haggard D., Nynka M., Ruan J. J., Kalogera V., Cenko S. B., Evans P., Kennea J. A., 2017, ApJ, 848, L25

Hallinan G. et al., 2017, Science, 358, 1579

Hotokezaka K., Kiuchi K., Kyutoku K., Okawa H., Sekiguchi Y.-i., Shibata M., Taniguchi K., 2013, Phys. Rev. D, 87, 024001

Hotokezaka K., Wanajo S., Tanaka M., Bamba A., Terada Y., Piran T., 2016, MNRAS, 459, 35

Just O., Bauswein A., Pulpillo R. A., Goriely S., Janka H.-T., 2015, MNRAS, 448, 541

Kasen D., Badnell N. R., Barnes J., 2013, ApJ, 774, 25

Kasen D., Fernandez R., Metzger B., 2015, MNRAS, 450, 1777

Kasen D., Metzger B., Barnes J., Quataert E., Ramirez-Ruiz E., 2017, Nature, 551, 80 EP

Kasliwal M. M. et al., 2017, Science, 358, 1559

Kawaguchi K., Shibata M., Tanaka M., 2018, preprint (arXiv:1806.04088)

Kilpatrick C. D. et al., 2017, Science, 358, 1583

Kulkarni S. R., 2005, ArXiv Astrophysics e-prints

Lattimer J. M., Schramm D. N., 1974, ApJ, 192, L145

Lehner L. et al., 2016, Class. Quantum Gravity, 33, 184002

Li L.-X., Paczynski B., 1998, ApJ, 507, L59

Lipunov V. M. et al., 2017, ApJ, 850, L1

Mao J., Kaastra J., Badnell N. R., 2017, A&A, 599, A10

Margalit B., Metzger B. D., 2017, ApJ, 850, L19

Margutti R. et al., 2017, ApJ, 848, L20

Martinez J. G. et al., 2015, ApJ, 812, 143

McCully C. et al., 2017, ApJ, 848, L32

Metzger B. D., 2017, Living Rev. Rel., 20, 3

Metzger B. D., Fernandez R., 2014, MNRAS, 441, 3444

Metzger B. D., Piro A. L., Quataert E., 2008, MNRAS, 390, 781

Metzger B. D. et al., 2010, MNRAS, 406, 2650

Metzger B. D., Bauswein A., Goriely S., Kasen D., 2015, MNRAS, 446, 1115

Metzger B. D., Thompson T. A., Quataert E., 2018, ApJ, 856, 101

Most E. R., Weih L. R., Rezzolla L., Schaffner-Bielich J., 2018

Nicholl M. et al., 2017, ApJ, 848, L18

Oechslin R., Janka H.-T., Marek A., 2007, A&A, 467, 395

Perego A., Rosswog S., Cabezón R. M., Korobkin O., Käppeli R., Arcones A., Liebendörfer M., 2014, MNRAS, 443, 3134

Perego A., Radice D., Bernuzzi S., 2017, ApJ, 850, L37

Pian E. et al., 2017a, Nature, 551, 67

Pian E. et al., 2017b, Nature, 551, 67 EP

Piro A. L., Kollmeier J. A., 2018, ApJ, 855, 103

Pürrer M., 2014, Class. Quantum Gravity, 31, 195010

Radice D., Galeazzi F., Lippuner J., Roberts L. F., Ott C. D., Rezzolla L., 2016, MNRAS, 460, 3255

Radice D., Perego A., Zappa F., Bernuzzi S., 2018, ApJ, 852, L29

Rezzolla L., Kumar P., 2015, ApJ, 802, 95

Roberts L. F., Kasen D., Lee W. H., Ramirez-Ruiz E., 2011, ApJ, 736, L21

Roberts L. F. et al., 2017, MNRAS, 464, 3907

Rosswog S., Liebendörfer M., Thielemann F.-K., Davies M. B., Benz W., Piran T., 1999, A&A, 341, 499

Rosswog S., Sollerman J., Feindt U., Goobar A., Korobkin O., Fremling C., Kasliwal M. M., 2017a, A&A, 615, A132

Rosswog S., Feindt U., Korobkin O., Wu M.-R., Sollerman J., Goobar A., Martinez-Pinedo G., 2017b, Class. Quantum Gravity, 34, 104001

Sekiguchi Y., Kiuchi K., Kyutoku K., Shibata M., 2015, Phys. Rev. D, 91, 064059

Shappee B. J. et al., 2017, Science, 358, 1574

Shibata M., Taniguchi K., 2006, Phys. Rev. D, 73, 064027

Shibata M., Fujibayashi S., Hotokezaka K., Kiuchi K., Kyutoku K., Sekiguchi Y., Tanaka M., 2017, Phys. Rev. D, 96, 123012

Siegel D. M., Metzger B. D., 2017

Siegel D. M., Ciolfi R., Rezzolla L., 2014, ApJ, 785, L6

Smartt S. J. et al., 2015, A&A, 579, A40

Smartt S. J. et al., 2017, Nature, 551, 75

Soares-Santos M. et al., 2017, ApJ, 848, L16

Tanaka M., 2016, Adv. Astron., 2016, 6341974

Tanvir N. R. et al., 2017, ApJ, 848, L27

Troja E. et al., 2017, Nature, 551, 71

Utsumi Y. et al., 2017, PASJ, 69, 101

Valenti S. et al., 2017, ApJ, 848, L24

Villar V. A. et al., 2017, ApJ, 851, L21

Wanajo S., Sekiguchi Y., Nishimura N., Kiuchi K., Kyutoku K., Shibata M., 2014, ApJ, 789, L39

Waxman E., Ofek E., Kushnir D., Gal-Yam A., 2017, preprint (arXiv:1711.09638)

Wollaeger R. T. et al., 2018, MNRAS, 478, 3298

Wu M.-R., Fernández R., Martínez-Pinedo G., Metzger B. D., 2016, MNRAS, 463, 2323

SUPPORTING INFORMATION

Supplementary data are available at *MNRAS* online.

Please note: Oxford University Press is not responsible for the content or functionality of any supporting materials supplied by the authors. Any queries (other than missing material) should be directed to the corresponding author for the article.

This paper has been typeset from a TEX/LATEX file prepared by the author.